Journal of Materials Chemistry C

Accepted Manuscript

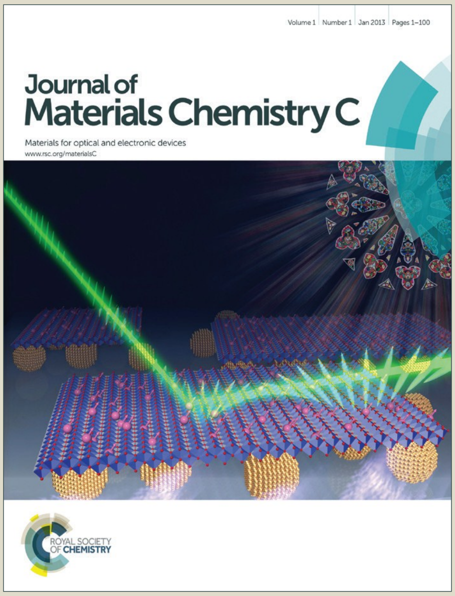

ROYAL SOCIETY OF CHEMISTRY

www.rsc.org/materialsC

Journal of Materials Chemistry C

ARTICLE

Decoration of nanocarbon solids with magnetite nanoparticles: towards microwave metamaterial absorbers

Received 00th January 20xx,
Accepted 00th January 20xx

DOI: 10.1039/x0xx00000x

www.rsc.org/

Francisco Mederos-Henry[a], Benoît P. Pichon[b], Yzaora Tchuitio Yagang[a], Arnaud Delcorte[c], Christian Bailly[c], Isabelle Huynen*[d] and Sophie Hermans*[a]

Three methods for decoration of nanocarbon solids (NcS) with magnetite nanoparticles (MaNPs) were compared, namely covalent linkage, direct co-precipitation or solvothermal synthesis. The influence of each method on the obtained nanocomposites most relevant characteristics were studied, such as chemical identity, size, loading rate and spatial distribution of the MaNPs over the NcS. The impact of the variables controlling the solvothermal decoration of a wide variety of NcS was investigated in more detail, such as the nature of the iron precursor and the NcS (type and oxidation state), the reaction temperature, time and water content. Finally, the obtained nanocomposites' superparamagnetic MaNPs were found to induce a ferromagnetic resonance (FMR) phenomenon, imparting a natural or zero-field resonance around 4 GHz. It was also demonstrated that the amount of loaded MaNPs had an effect on the FMR absorption intensity as well as on the nanocomposites electrical properties. The latter were also shown to be governed by the chosen NcS type. These features could easily be exploited as control mechanisms to construct highly effective microwave metamaterial absorbers possessing low incident microwave reflection and maximal absorption rate.

1. Introduction

Metamaterials (MMs) are artificial materials exhibiting unconventional electromagnetic (EM) properties that cannot be found in nature, such as a negative refractive index and the backward propagation of waves [1, 2]. Since their first experimental demonstration by Smith *et al.* [3], a wide variety of applications has been proposed for these materials in the microwave range. Of particular interest is their use as perfect microwave absorbers that could be used as highly efficient EM shielding materials [4, **Error! Reference source not found.**].

The absorbance *A* of a MM can be maximized if one can simultaneously minimize its transmission *T* and reflection given that

$$A = 1 - R - T \quad (1)$$

Very low *T* can be achieved by inducing losses in the material, described by the imaginary components of the complex electric permittivity, $\varepsilon(\omega)$, and magnetic permeability, $\mu(\omega)$, factors. Similarly, R can be minimized by matching the free space impedance, Z_o, to the MM impedance $Z(\omega)$, defined as

$$Z(\omega) = \sqrt{\mu(\omega)/\varepsilon(\omega)} \quad (2)$$

It is thus evident that the independent manipulation of both ε and μ is necessary to modify the MMs absorption behaviour.

ε and μ-tunable metamaterial structures have mostly been produced by organizing dielectric and conductive material constituents in a highly controlled fashion [7]. For instance, micrometric elements acting as resonant cells are usually fabricated by techniques derived from (micro)electronics production, such as circuit printing [3, 5]. Even though this method is nowadays widely available and inexpensive, some important limitations arise when it is applied to metamaterials production for real-life applications.

Indeed, achieving the desired electromagnetic properties using printed circuit units imposes constraints on the end product size and shape [5]. Alternatives such as shadow photolithographic mask/etching methods in the visible or ultraviolet range or electron/laser beam lithography have also been explored [7], especially when nanometric components are sought. Even though these techniques can effectively alleviate some of the above-mentioned drawbacks, it is practically impossible to use them in large-scale production. Indeed costly instruments are usually required, production

---

[a] *Institute of Condensed Matter and Nanosciences (IMCN), Division of Molecules, Solids and Reactivity (MOST), Place Louis Pasteur 1, Université catholique de Louvain, B-1348 Louvain-la-Neuve, Belgium. *E-mail : Sophie.Hermans@uclouvain.be.*

[b] *Institut de Physique et Chimie des Matériaux de Strasbourg, UMR CNRS-UdS 7504, 23 rue du Loess – BP 43, 67034 Strasbourg Cedex 2, France.*

[c] *Institute of Condensed Matter and Nanosciences (IMCN), Division of Bio and Soft Matter (BSMA), Croix du Sud 1, Université catholique de Louvain, B-1348 Louvain-la-Neuve, Belgium.*

[d] *Institute of Information and Communication Technologies, Electronics and Applied Mathematics (ICTEAM), Place du Levant 3, Université catholique de Louvain, B-1348 Louvain-la-Neuve, Belgium. *E-mail : isabelle.huynen@uclouvain.be*

Electronic Supplementary Information (ESI) available: 1) Reactants specifications; 2) Covalent linkage of functionalized core-shell nanoparticles and graphene oxide acyl chloride derivative (COV); 3) TEM images of tethered core-shell nanoparticles. 4) Oxygenated functions abundance in the different graphenic solids as determined by XPS; 5) TGA analysis of a series of samples synthesized by the SOLV-A method. See DOI: 10.1039/x0xx00000x times are lengthy and usually only one component can be manufactured at a time.

An attractive and increasingly explored alternative to the “circuit fabrication” approach to metamaterials is the “chemical buildup” route [7]. Indeed, chemically driven organization of electromagnetically active constitutive units has the potential to yield metamaterial structures in larger quantities at reduced costs. However, it is considered that chemical methods have a major drawback: they naturally produce disordered and randomly distributed objects. Structural disorder reduces the intensity of a resonant phenomenon or shifts its frequency [7], induces a narrow-band operation or increases the material’s dispersivity and loss [8].

We are currently developing a new generation of microwave metamaterial absorbers in which these losses are intentionally used to design highly efficient microwave absorbing devices. In our approach, a nanocarbon solid (NcS) that has been decorated with magnetic nanoparticles is dispersed in a host polymeric matrix [9], offering a flexible assembly framework, from the nano to the micrometric scales, in which the different components’ composition, concentration and spatial distribution can be adjusted to finely tune the MM effective $\varepsilon(\omega)$ and $\mu(\omega)$ values.

Nanocomposites obtained by decoration of NcS with magnetite nanoparticles (MaNPs) have already been reported in the scientific literature for very diverse applications such as the production of energy storage devices [10, 12], the remediation of environmental pollutants [14, 15], the design of controlled drug carriers [16] or biosensors [17], to mention just a few. However, up to this date, there is no evidence that any such nanomaterial has been tested as a microwave-responsive metamaterial. Their microwave absorbing properties have already been acknowledged and partially investigated [18, 19], restricted however to a Jaumann configuration where frequency-selective absorbing performance is primarily controlled by the thickness of the sample, while a ferromagnetic resonance (FMR) mechanism has not been evidenced nor exploited to induce losses in such materials.

Most commonly, these magnetite/carbon nanocomposites have been produced through solvothermal [10, 20-22] or hydrothermal [12, 13] strategies, direct co-precipitation of iron (II) and (III) salts on the NcS [15, 23], the covalent bonding of nanoparticles onto the NcS [14, 24] or thermal decomposition of an iron precursor [25]. As far as we know, no study has yet been published on the comparative advantages and drawbacks that each technique offers. Instead, only a few general challenges faced during the creation of these materials have been mentioned [14, 26], such as reaching a tight control over the MaNPs loading rate, anchoring them strongly to the NcS to avoid leaching or distributing them homogeneously over the NcS surface.

In this study, we compare nanocomposites obtained either by the covalent linkage of MaNPs to graphene oxide (GO), or their deposition onto this NcS by a direct coprecipitation or a solvothermal strategy. Our aim is to obtain for the first time a direct comparison of these three synthetic methods with the same nano-carbon solid. More particularly, we compare chemical identity, size, loading rate and spatial distribution of the nanoparticles deposited over the NcS in each case. In order to go beyond the state-of-the-art in the field, and to obtain a tight control over the final characteristics of the nanocomposites obtained, we studied the solvothermal method more thoroughly to unravel the key parameters that can be fine-tuned in a predictive manner to obtain the desired materials. The goal of the present study was not to carry out a systematic study of each experimental parameter for the three different synthetic methods, but to identify how to attain control of the final materials to explore their EM properties to obtain reliable structure/activity relationships.

The magnetic properties of the obtained materials were studied using SQUID. Finally, the milestone towards effective metamaterial absorbers is to observe experimentally an FMR phenomenon directly on the powders. This, as far as we know, as never been done on such nanocomposites. These results would prove that the MaNPs allow us to introduce lossy resonances in the frequency response of the system’s magnetic permeability. The controlled synthesis of these nanocomposites can thus be considered as a first step towards the design of highly efficient microwave absorbers.

2. Results and discussion

Three different synthetic approaches were used to produce a series of MaNPs@NcS nanocomposites, where NcS are carbon nanotubes or graphenic powders (see Table 1). The obtained MaNPs@NcS nanocomposites were extensively characterized in order to identify the influence of experimental parameters on the obtained nanocomposites physicochemical characteristics. Accordingly, TGA analyses allowed quantifying the amount loaded onto a NcS. SEM-EDX and TEM analyses permitted to assess the nanoparticles morphology, size and spatial distribution over the NcS surface. XRD was used to determine the nature and purity of the iron-containing phase(s). Finally, in the case of the covalent linkage of the MaNPs to GO, XPS allowed us to prove that these particles were effectively anchored to the functionalized surface by means of an amide covalent bond (see ESI, section 2), indicating that all the intermediate synthetic steps were successfully accomplished.

2.1 Comparison of MaNPs@GO nanocomposites obtained by the solvothermal (SOLV-A), direct co-precipitation (DCOP) and covalent linkage (COV) methods.

Graphene oxide (GO) was decorated with magnetite nanoparticles (to give MaNPs@GO nanocomposites) using direct co-precipitation, solvothermolysis and covalent bonding techniques. Our findings demonstrate that the most relevant characteristics of the obtained nanocomposites, namely chemical identity, size, loading rate and spatial distribution of the nanoparticles over the NcS, are strongly determined by the chosen synthetic method.

Similar cuboidal or elongated prismatic morphologies were observed in all the MaNPs deposited onto or covalently attached to GO. However, the measured average particle sizes and particle size distributions were different for each technique. The MaNPs found in the DCOP nanocomposite (Fig. 1b) are the smallest and their size distribution is the narrowest. On the contrary, those directly co-precipitated in the absence of any NcS (Fig. 1a), used later for the COV product, were larger and possessed wider size distributions, revealing a templating effect of the NcS as previously claimed [18, 28-30]. The SOLV-A method (Fig. 1c) also produced larger particle sizes and wider size distributions than those obtained for the DCOP nanocomposite, possibly due to the higher temperatures and longer reaction times used.

In terms of the deposited nanoparticles' phase composition, the solvothermal strategy systematically produced an iron oxide phase with the spinel structure. Rietveld refinement analyses of XRD data were performed in order to determine the contribution of magnetite and maghemite. In all cases, the latter product was found to be a subsidiary phase (<2%), possibly present as a magnetite@maghemite core@thin shell structure as observed by Baaziz *et al*. [27]. Thus, for practical purposes, we herein assume the nanoparticles to be mostly pure magnetite (Fig. 2a). By opposition, the direct co-precipitation method led to a lepidocrocite contamination (Fig. 2b), whose amount varies from batch to batch (Fig. 2b dotted line for a repeated synthesis). This type of impurity had already been observed by other authors [31-32]. Oxyhydroxides impurities are problematic for our intended applications given that they are non-magnetic and can readily transform into other iron-containing species [33]. If present, no real control over the end-product composition and its resultant electromagnetic properties can be expected.

When considering the known chemistry of iron oxides, hydroxides and oxyhydroxides, it becomes clear that the direct co-precipitation (DCOP) approach, known as the classical magnetite synthesis, might not be the best choice if a pure Fe_3O_4 phase is desired. Indeed, it is evident that the DCOP experimental conditions can easily lead to the formation of parasitic phases via undesired iron-containing species, due to the simultaneous presence of Fe(II) and Fe(III) ions [31-34]. This is even worse if oxygen has not been well evacuated from the reaction atmosphere [32, 35] or if the Fe(II)/Fe(III) molar ratio is not strictly kept at a value of 0.5 [32].

Each methodology also produced significantly different spatial distribution of the MaNPs over the NcS. In the case of the covalent linkage strategy, we observed that functionalized silica-coated MaNPs were randomly distributed all over the graphenic sheets (Fig. 3a,b), as well-individualized particles or nanosized agglomerates (Fig. 3c).

Table 1 Overview of the different synthetic methods used in this study

Synthetic method	Codename	Nanocarbon solid used	Iron precursor used	Characterization techniques
Covalent linkage	COV	Acyl-functionalized GO	$FeCl_2•4H_2O$ $FeCl_3•6H_2O$	XRD, SEM-EDX, TEM, XPS
Direct co-precipitation	DCOP	GO	$FeCl_2•4H_2O$ $FeCl_3•6H_2O$	XRD, SEM-EDX, TEM, TGA
Solvothermolysis	SOLV-A	GO, GNPs MWCNTs, ox-MWCNTs	$FeCl_3•6H_2O$	XRD, SEM-EDX, S-parameters, SQUID, TEM, TGA.
	SOLV- B	GO	$Fe(acac)_3$	XRD, SEM-EDX, TEM, TGA
	SOLV- C	GO, rGO, GNPs	$Fe(acac)_3$	
	SOLV- D	MWCNTs, GNPs	$Fe(acac)_3$	

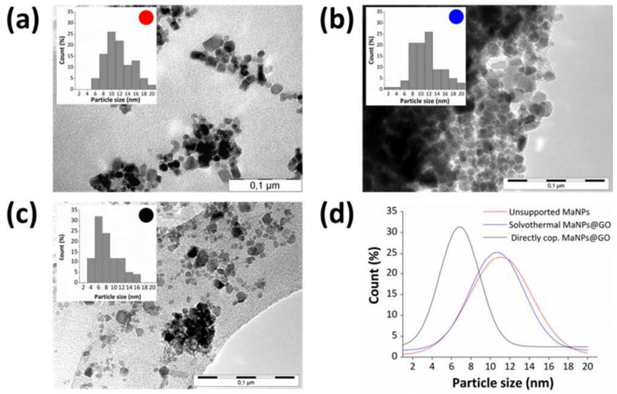

Fig. 1 TEM images and (inset) histograms of particle size distribution of (a) unsupported MaNPs used for the COV method, (b) solvothermally deposited MaNPs@GO and (c) directly co-precipitated MaNPs@GO nanocomposites; (d) Gaussian-function fitting of experimental particle size data.

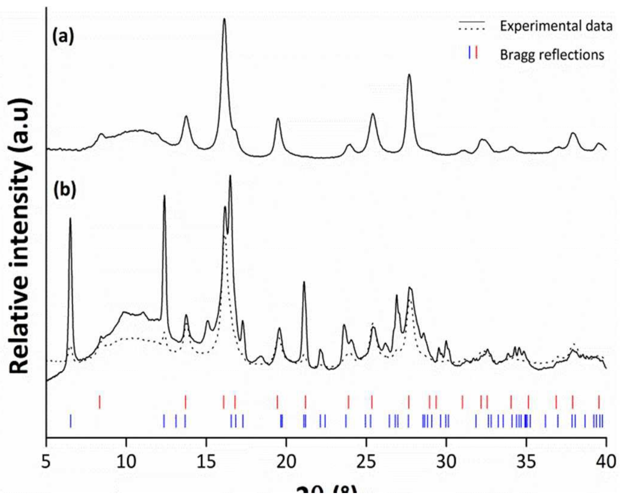

Fig. 2 XRD diffraction patterns of MaNPs@GO nanocomposites obtained by (a) SOLV-A and (b) DCOP strategies. In the case of the latter, the synthesis was repeated (dotted black line). Red and blue lines indicate Bragg reflections belonging to magnetite and lepidocrocite phases respectively.

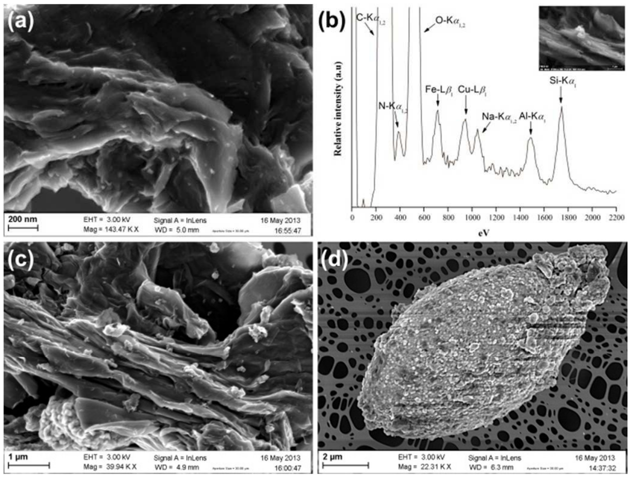

Fig. 3 (a) SEM image of the end product resulting from the multi-step covalent linkage methodology; (b) EDX spectrum obtained from a particle (inset picture): Fe, Si and N signals confirm the presence of functionalized silica-coated MaNPs. Cu and Al signals belong to the sample holder while the presence of Na can be traced back to the synthesis of the unsupported MaNPs; (c) SEM image of individualized and nanosized agglomerates attached to the graphenic surface; (d) SEM image of large micrometric agglomerates.

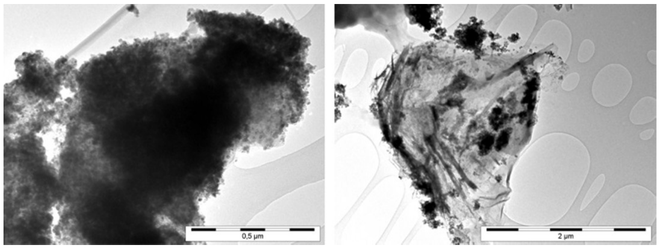

Fig. 4 TEM images of (left) the solvothermal and (right) the direct co-precipitation products.

However, much larger micrometric aggregates coexist independently of the NcS (Fig. 3d), composed of magnetite-silica core-shells nanoparticles agglomerated by means of magnetic dipole-dipole interactions. These large, independent, agglomerates can locally modify the resultant metamaterial's electromagnetic behavior and are thus undesirable.

The SOLV-A strategy produced a nanocomposite in which the NcS was homogeneously and densely decorated with MaNPs, while in the product obtained by direct co-precipitation, the particles seemed to randomly agglomerate on certain areas of the NcS (Fig. 4).

The observed difference in the nanoparticles' spatial distributions is possibly related to the interaction between the graphenic surface and the intermediate species formed in each case, as explained below.

Under the experimental conditions used in the DCOP synthesis, the initial pH value is low (pH=2.0). Only a slight fraction of GO's carboxylic acid groups are expected to be ionized [36]. In consequence, a minor percentage of the total positively charged iron ions species is in close contact with the graphenic surface, while the rest remains in the bulk solution. Once the pH is raised to 10, magnetite particles begin to form, both over the GO's surface and in solution. Given the strong magnetic dipole-dipole interactions existing between MaNPs crystallites [27], the particles formed on the nanocarbon surface attract those precipitating from solution, causing them to agglomerate.

In the case of the solvothermal strategy, the early creation of a strongly basic reaction medium not only causes the formation of diverse $Fe_xO_yH_z$ species [10, 31], but also deprotonates a larger number of GO's acidic groups than under the DCOP conditions [36]. This confers a net negative charge to the NcS surface [36] hence causing electrostatic attraction for iron species from solution. Thus, once the solvothermal reaction starts, the formed MaNPs tend to distribute evenly along the graphenic sheets.

Concerning the MaNPs loading rate, the solvothermal procedure comparatively offers a much simpler way of modifying the amount of MaNPs that can be loaded onto the NcS by simply adjusting the amount of Fe(III) precursor engaged in the reaction. However, the direct co-precipitation method allows for slightly higher mass Fe/GO loadings than the solvothermal approach: 37% loading rate for the former versus 33% for the latter (50% intended), with the same graphene oxide NcS. The amount of covalently linked MaNPs is considerably inferior to the ones obtained with the two other techniques.

Table 2 Experimental conditions of the different solvothermal methods considered

Method	NcS	Iron Precursor	Solvent mixture / % v/v	Temperature / ºC	Time
SOLV-A	GO, GNPs MWCNTs, ox-MWCNTs	$FeCl_3•6H_2O$	50% EG 25% PEG-400 25% Water	180	24 h
SOLV- B	GO	$Fe(acac)_3$	80% EG 20% Water	260	80 min
SOLV- C	GO, rGO, GNPs	$Fe(acac)_3$	EG	180	16 h
SOLV- D	MWCNTs, GNPs	$Fe(acac)_3$	TREG	250	40 min

2.2 Influence of the solvothermal experimental parameters on the nanocomposite characteristics.

According to the results presented above, the nanocomposites produced *via* the solvothermal strategy are more homogeneous and tunable, hence more appropriate for our targeted applications. In consequence, we tested different solvothermal procedures (see Experimental section and Table 2) in which the nanocarbon solid and its degree of oxidation, the nature of the iron precursor, the composition of the solvent mixture, the reaction temperature and time as well as the amount of water present in the system were varied. The goal is to pinpoint the impact of each experimental parameter on the final nanocomposites characteristics.

2.2.1 Deposited nanoparticles' chemical identity, morphology and particle size. Pure magnetite crystallites were identified by XRD in the products obtained by all four solvothermal methods. No other iron-containing parasitic phases were detected in any case. However, for identical loading rates of 50% Fe/NcS and independently of the NcS used, important differences where observed between the samples produced with the $FeCl_3•6H_2O$ salt or the $Fe(acac)_3$ complex (Fig. 5). In the case of the former, all characteristic magnetite reflections are present while, in the case of the later, only the most intense reflections stand out from the background. Furthermore, at low loading rates, e.g. 10% Fe/NcS, signals were still detectable for nanocomposites produced with the iron salt precursor while only signals corresponding to the NcS could be observed in samples synthetized using the iron complex. The striking difference in signal intensity was found to be due to both, the crystallites size as well as their abundance.

Indeed, TEM inspection of the obtained nanocomposites revealed that the iron precursor nature produces a significant difference in the size of the deposited MaNPs. Independently of the NsC used, samples produced using the iron salt were composed of prismatic magnetite nanoparticles with average sizes comprised between 8 and 13 nm approximately (Table 3). Instead, in the samples produced with the iron complex, the deposited MaNPs were difficult to observe given their extremely reduced size: the average particle size did not exceed 2.6 nm. Nonetheless, a similar prismatic morphology was also observed in those rare particles of larger size that were found in these samples.

In the scientific literature [33], reaction time and temperature are usually regarded as the main critical factors controlling the obtained MaNPs size. However, our findings indicate that the obtained size differences cannot be attributed to reaction temperature. Indeed, as shown in Table 2, the iron complex is exposed to identical or higher reaction temperatures in methods SOLV-C or SOLV-D respectively, than the iron salt precursor in method SOLV-A. Nonetheless, as mentioned above, MaNPs found in SOLV-A products are from six to ten times larger (Table 3) than those obtained by the SOLV-C or SOLV-D methods, considering a same NcS and an identical intended Fe/NcS loading rate (LR).

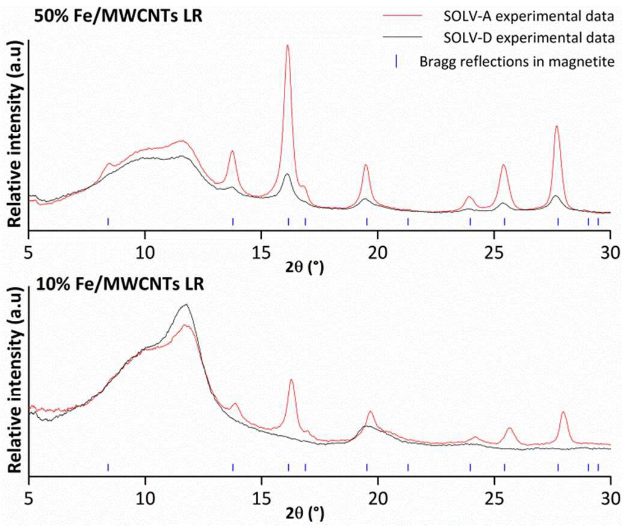

Fig. 5 XRD diffractograms of MaNPs@MWCNTs produced with methods using an iron salt (SOLV-A) and an iron complex (SOLV-D) precursor at different Fe/NcS loading rates. Blue lines indicate Bragg reflections belonging to magnetite.

Another critical factor that seems to govern the deposited MaNPs particle size is the amount of water included in the reaction mixture, as proven by the results obtained with the SOLV-B method. In this approach, $Fe(acac)_3$ is also used as the iron precursor and its reaction conditions combine those used in methods SOLV-C and SOLV-D except that 20% (v/v) water is included in the reaction media. As shown in Table 3, for the same NcS and intended LR, the deposited MaNPs size (5.8 ± 2.1 nm) is almost five times the size obtained using the SOLV-C method (1.3 ± 1.8 nm), notwithstanding the much shorter reaction times used in method SOLV-B.

Determining why water has such an important effect on the deposited MaNPs size requires an understanding of the mechanism underlying the polyol solvothermal decomposition of $Fe(acac)_3$ and its transformation to magnetite. Even though some limited explanations regarding this particular reaction system can be found in the work of Deng *et al.* [21], a thorough mechanistic study has yet to be performed.

Table 3 Influence of the solvothermal method experimental conditions on the average size of MaNPs deposited onto different NcS as measured by TEM.

Method	SOLV-A			SOLV-B	SOLV-C		SOLV-D	
NcS	MWCNTs	ox-MWCNTs	GO	GO	GO	GNPs	GNPs	MWCNTs
% Fe/NcS LR	50%	50%	10%	10%	10%	10%	10%	50%
Avg. size / nm	13.2 ± 5.9	8.5 ± 3.3	11.0 ± 3.9	5.8 ± 2.1	1.3 ± 1.8	2.2 ± 1.0	1.8 ± 1.0	2.0 ± 2.9

Nonetheless, it is known that water plays an essential role in the hydrolysis reactions leading to the formation of intermediary hydroxide and oxyhydroxides species [33] that could be involved in the formation of magnetite under the used solvothermal reaction conditions. Thus, its presence in larger quantities than those produced by the thermal decomposition of the glycol moieties [21, 37] would seem to yield larger amounts of magnetite available for crystal nucleation and growth onto the NcS. Whatsoever, the total amount of water in the system should be kept below 60% (v/v %). Indeed, it has been shown [21] that, in similar reaction systems, a hematite phase is formed when water exceeds this concentration limit.

Another factor that has a non-negligible effect on the deposited MaNPs size is the oxidation degree of the NcS. Results shown for SOLV-A and SOLV-C methods in Table 3 indicate that the MaNPs size decreases as the number of oxygenated functions on the NcS surface increases, both in carbon nanotubes and in graphenic solids, independently of the type of iron precursor used. These results would tend to prove that, after electrostatically attracting the iron-containing species existing in the reaction mixture, the solid's oxygenated functions serve as nucleation sites to the forming MaNPs. Thus, the higher density of oxygenated functions on the surface of the NcS produces a higher nucleation rate and the resulting particle size decreases, as observed. The formation of Fe-O-C bonds between Fe_3O_4 and a NcS surface through the latter's oxygenated functions has been considered [25, 38] to explain the stabilization of deposited MaNPs toward excessive sintering when similar MaNPS@graphene nanocomposites were subjected to thermal annealing. In this case, our results prove that the NcS' oxygenated functions can also be used to tune the deposited MaNPs size.

2.2.2 MaNPs loading rate. The amount of MaNPs that can be loaded solvothermally onto a NcS seems to depend on the nature of both, the iron precursor and the NcS itself.

For instance, TGA results showed that independently of the NcS, a lower Fe/NcS LR was systematically obtained when the $Fe(acac)_3$ complex was used as an iron precursor in methods SOLV-C or SOLV-D (see Table 4). Moreover, a similar thermal event spanning between 200 ºC and 400 ºC was observed in all the TGA profiles of the SOLV-C and SOLV-D products. This temperature range matches the one observed during the thermal decomposition of the iron complex itself (Fig. 6), suggesting that, under these reaction conditions, the iron precursor is only partially decomposed. Accordingly, when aiming a 50% Fe/NcS LR, a similar amount (approx. 25%) of partially decomposed complex was found in all SOLV-C nanocomposites, independently of the used NcS, being slightly lower (19%) in the SOLV-D products. These results can be attributed to the lower reaction temperature used in the SOLV-C approach, which lead to a higher rate of remaining undecomposed complex.

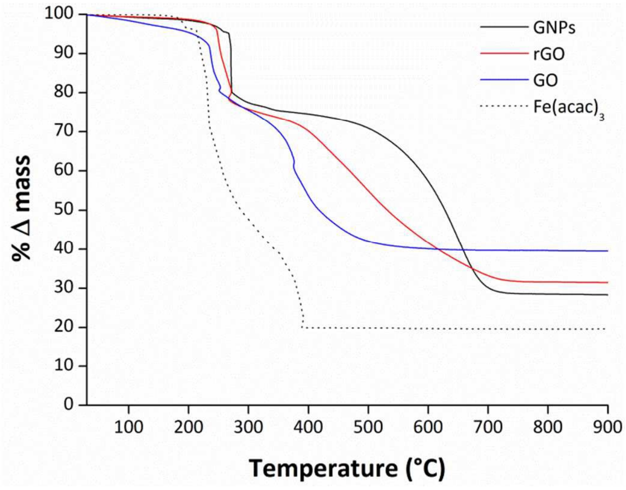

Fig. 6 Thermograms for the thermal decomposition under air of a $Fe(acac)_3$ reference sample and three SOLV-C nanocomposites produced using different NcS and an intended 50% Fe/NcS loading rate.

As shown in Table 4, when applying the SOLV-A methodology to ox-MWCNTs and MWCNTs, aiming a 50% Fe/NcS LR, it was found that the obtained value was slightly higher for the oxidized sample (21%) than for its non-oxidized counterpart (18%). Using the same synthetic conditions, a more accentuated difference was found when comparing the loading rate obtained for GO (37%) and GNPs (29%). A similar trend was also observed when decorating GO, rGO or GNPs using the SOLV-C approach. In this case, while aiming for a 50% Fe/NcS LR in all products, the obtained LR was the highest for the GO product (19%), followed by rGO (15%) and lowest when using GNPs (13%) (Fig. 6), in agreement with the decreasing amount of oxygenated functions found in these graphenic solids as determined by XPS (see ESI, section 3). These results indicate that the oxygenated functions also have an influence on the MaNPs loading rate and not only on their size. As mentioned before, an electrostatic interaction is established between the oxygenated functions present on the NcS and some of the iron-containing species found in solution. This interaction would be responsible for bringing both components in close contact before and during the formation of MaNPs, generating a higher LR as the concentration of oxygenated functions on the NcS increases. The higher loading rates observed in the SOLV-A products could also be due to the basic pH values used in this methodology. Indeed, as

Table 4 Amounts of loaded iron onto different NcS determined by TGA analysis (50% Fe/Ncs LR aimed at)

Method	SOLV-A				SOLV-C			SOLV-D	
NcS	MWCNTs	ox-MWCNTs	GO	GNPs	GO	rGO	GNPs	GNPs	MWCNTs
% Fe/NcS LR	18	21	37	29	19	15	13	13	12

mentioned before, such a basic environment would produce a higher concentration of ionized oxygenated species and thus increase the extent of electrostatic interactions.

The overall effective surface of the different NcS also seems to influence the obtained Fe/NcS LR. Indeed, textural analysis by nitrogen physisorption of GO and GNPs indicate a much higher specific surface area for the former NcS than for the latter (50 m^2/g and 16 m^2/g respectively, similar to the values observed in [39]). This difference can be explained in terms of the degree of graphene sheet stacking present in each NcS sample. Indeed, our XRD and TEM results confirm that the GNPs are composed of highly stacked graphenic sheets while in GO these are more individualized.

As mentioned before, one of the advantages of the solvothermal approach is that the amount of loaded MaNPs onto the NcS can be easily modified. Using the SOLV-A method, the amount of $FeCl_3$•$6H_2O$ was adjusted to create a series of nanocomposites with Fe/GO LRs varying from 10% to 50%. The TGA analyses of such nanocomposites indicate that an excellent correlation between the expected and obtained LRs was maintained up to loadings of 30% (Fig. 7). At higher LR, a saturation plateau seems to be reached. Nonetheless, in all cases, this method proved to produce highly reproducible loading rates (see ESI, section 4).

2.2.3 MaNPs spatial distribution over the NcS surface. As described before, when compared to the DCOP and COV linkage methodologies, the solvothermal strategy produced, at high Fe/NcS LR (e.g. 50%), a nanocomposite in which the NcS was homogeneously and densely decorated with MaNPs. Nanocomposites of lower Fe/NcS LRs, ranging from 10% to 40%, were also produced using the SOLV-A methodology. The SEM and TEM inspection of these five products revealed that the spatial distribution over the NcS surface remained homogeneous in all cases (Fig. 8). It also showed that the MaNPs stacked less onto each other at lower LRs, forming what seemed localized single layers of MaNPs deposited onto the NcS surface (Fig. 8c). Nonetheless, it was also observed that some areas of the solid were left uncovered when engaging the lowest LR value (10%).

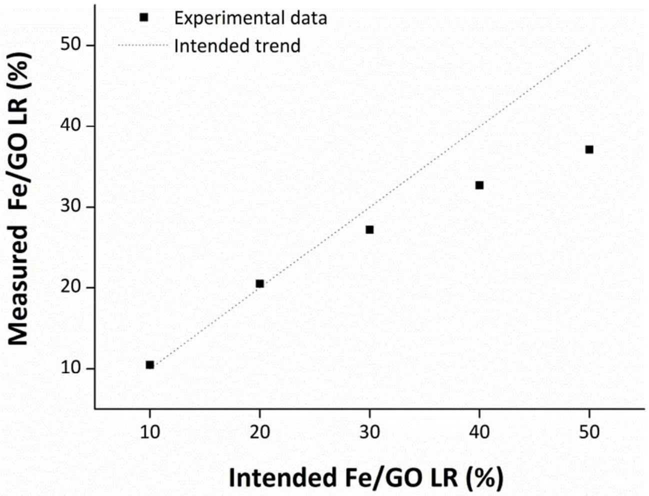

Fig. 7 Intended vs. measured (by TGA analysis) % Fe/GO loading rates (LR).

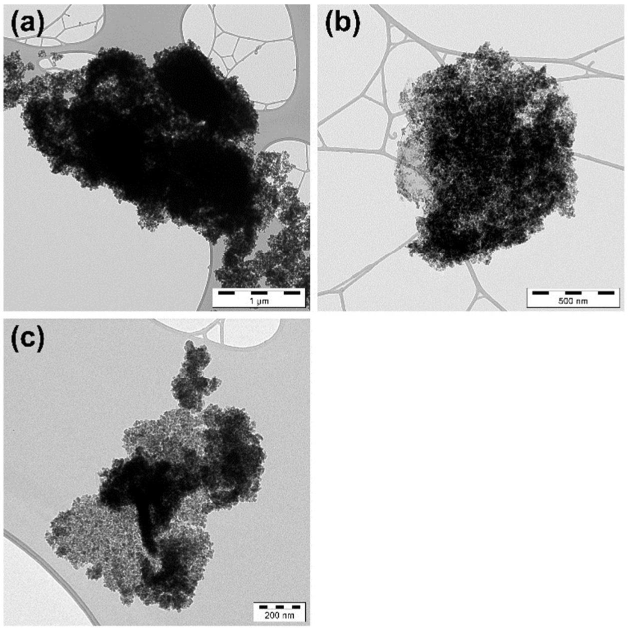

Fig. 8 TEM images of MaNPS@GO nanocomposites produced *via* the SOLV-A method at (a) 50%, (b) 30% and (c) 10% Fe/NcS LR.

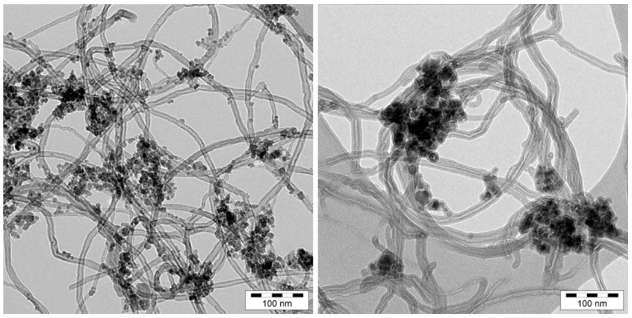

Fig. 9 TEM images of MaNPs deposited onto oxidized (right) or pristine (left) MWCNTs using the SOLV-A method.

The MaNPs spatial distribution was also affected by the presence of oxygenated functions on the NcS surface. This effect was highlighted when decorating pristine and oxidized MWCNTs using the SOLV-A method at a 10% LR value (Fig. 9). Indeed, smaller MaNPs distributed along the MWCNTs surface when these were previously oxidized, contrasted with only larger particle agglomerates found in the pristine MWCNTs samples. These results further prove that the NcS' oxygenated functions are serving as nucleation sites during the MaNPs formation and growth.

2.3 Characterization of the nanocomposites magnetic properties and microwave behavior. We characterized the nanocomposites' properties in the microwave range by measuring the scattering matrix and analyzing the values of the resulting transmission scattering parameter S_{21}.

It is worth mentioning that powder S-parameter characterization methodologies described in the scientific literature [e.g. 42-44] usually require the obtained materials to be mixed with a binder such as paraffin. Afterwards, the measurements are performed on standardized ring-like shaped structures of controlled thicknesses. Nonetheless, it is well known that the intensity and frequency of certain microwave phenomena, such as absorption, are strongly dependent on sample thickness [44]. Thus, under these conditions, the nanocomposites' inherent microwave responses are masked by the samples' thickness-derived effects, as it is impossible to differentiate one from another. By contrast, our measurements were directly performed on the nanocomposite powders, without any type of preliminary sample preparation, so that the obtained responses derivate exclusively from the studied nanocomposites.

Fig.10 shows the results for the S_{21} transmission parameter of a SOLV-A MaNPs@GO nanocomposite with an intended 50% Fe/NcS LR. A series of absorption processes are observed, which can be explained in terms of the ferromagnetic resonance (FMR) theory. Indeed, according to Kittel [45], the resonance frequency of a ferromagnetic material is dependent on the strength of an applied static magnetic field. This relationship is described by the so-called Kittel equation whose simplest expression for spherical particles is written as:

$$\omega_o = \gamma H_z \tag{3}$$

Where ω_o is the frequency at resonance, γ is the magneto-mechanical ratio for an electron spin (numerically, $\gamma/2\pi = 2.80$ megacycles/Oe) and H_z is the strength, in Oe, of a magnetic field applied perpendicularly to the sample.

In the case of zero static field (Hz=0) and if the MaNPs are large enough as to ensure a magnetic moment stability-lifetime, τ, superior to 10^{-9} s [46], an effective anisotropy field (H_a) is responsible for the so-called zero-field or natural resonance [45]. Under these conditions, the Kittel equation becomes:

$$\omega_o = \gamma H_a \tag{4}$$

Thus, in perfect agreement with what was experimentally observed here, this set of Kittel equations predicts the existence of a natural resonance, at zero magnetic field, that tends to shift toward higher frequencies as the applied magnetic field is increased. To the best of our knowledge, and given the sample preparation considerations stated above, this is the first time that the zero-field (4 GHz) and Hz-dependent FMR resonances are undoubtedly determined for this type of nanocomposites.

The FMR frequency depends on the chemical identity of the deposited NPs while its intensity can be controlled by modifying the Fe/NcS LR. Fig.11a compares the FMR behavior of the SOLV and DCOP nanocomposites described in section 2.1. For similar Fe/NcS LRs, the FMR absorption is more intense in the SOLV product given it contains only pure MaNPs while varying amounts of magnetite and lepidocrocite NPs are present in the DCOP powders. A similar trend is observed in Fig. 11b, showing the FMR behavior of SOLV-A MaNPs@GO nanocomposites with 10%, 30% and 50% intended Fe/NcS LRs. The absorption intensity sharply increases as a larger quantity of MaNPs is present.

The electrical properties of these materials also seem to be dependent on the amount of MaNPs loaded onto a particular NcS. As shown in Fig. 12, the relative permittivity (ε_r) and conductivity (σ) values for the 50% intended Fe/NcS LR MaNPs@GO nanocomposite are significantly lower than that of its 10% Fe/NcS LR counterpart. This is probably due to the insulating character of the magnetite phase. Furthermore, the materials' σ and ε_r values can be drastically modified by choosing a different NcS (see Fig. 13). In this case, by varying the NcS' oxidation degree (see ESI, section 4), one can modify the number of defects in the carbon network and thus impact its electron conductivity.

Finally, the magnetic properties of MaNPs@GO nanocomposites with 10%, 30% and 50% Fe/NcS LR produced by the SOLV-A method have been studied by SQUID magnetometry. Magnetization curves recorded against magnetic field, from one direction to the opposite one, show perfect overlapping at 300 K which corresponds to superparamagnetic behavior for all of them (Fig. 13a-c). In contrast, hysteresis loops exhibit coercive fields (H_c) of about 350 Oe at 5 K, which corresponds usually to ferrimagnetic iron oxide nanoparticles [40].

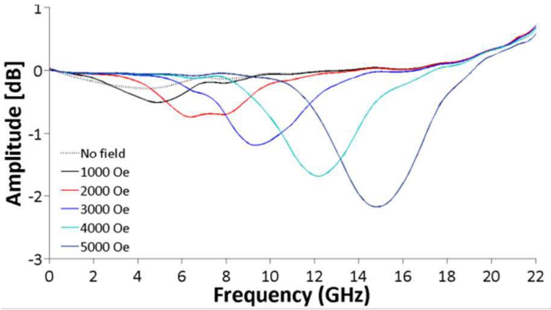

Fig. 10 FMR behaviour observed in S_{21} power transmission of a 50% Fe/NcS MaNPs@GO nanocomposite produced with the SOLV-A method.

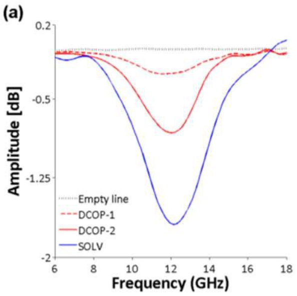

Fig. 11 FMR intensity response influenced by (a) purity of deposited NPs crystalline phase; (b) MaNPs loading rate onto NcS.

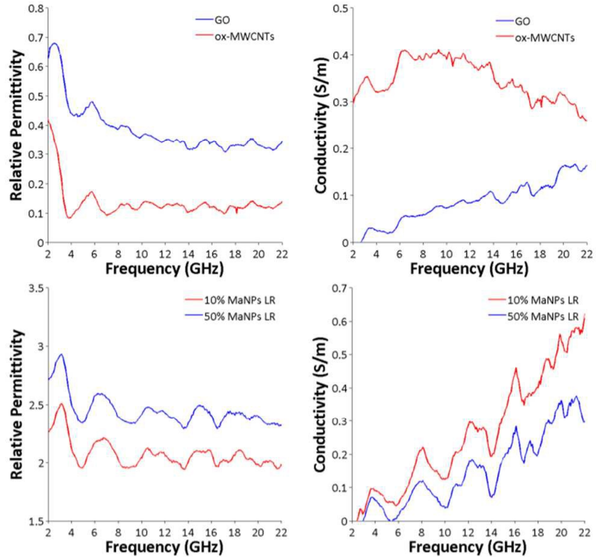

Fig. 12 Relative permittivity (left) and conductivity (right) for the 10% and 50% intended Fe/NcS LR MaNPs@GO nanocomposites produced with the SOLV-A method

Fig. 13 Relative permittivity (left) and conductivity (right) for 50% intended Fe/NcS LR MaNPs@GO or ox-MWCNTs nanocomposites produced with the SOLV-A method

Magnetization saturation values at 300 K also agree with the measured size of the nanoparticles (see Table 5). These values are much lower than bulk values for magnetite (92 emu/g) because of surface effects and the oxidation of Fe(II) at the nanoparticle's surface which generates vacancies and disorder [40]. The lowest Fe/NcS LR sample (10%) shows a lower H_c value which may be explained by larger surface effects or the presence of undetected slightly smaller nanoparticles.

In addition, temperature dependent magnetization (M(T)) curves (Fig. 13d) bring deeper information on the collective properties of nanoparticles. Zero field cooled (ZFC) curves exhibit a maximum at a temperature (T_{MAX}) whose value decreases with the density of MaNPs deposited on the NcS' surface (Table 5). Given the fact that the deposited MaNPs feature similar sizes, this decrease of T_{MAX} is correlated to weaker dipolar interactions due to larger interparticle distances. The non-saturation of the field cooled (ZF) curve at low temperature for the least loaded sample, in contrast to the other two samples, also confirms this result since it is correlated to the (quasi) absence of dipolar interactions as observed for iron oxide nanoparticles 2D assemblies [41].

Table 5 - Magnetic properties and average MaNPs sizes of 10%, 30% and 50% Fe/NcS samples produced *via* the SOLV-A method.

Fe/NcS LR	10%	30%	50%
M_S 300 K (emu/g)	46	61	61
H_C (Oe)	360	350	300
T_{MAX} (K)	135	248	290
Average particle size (nm)	11.0 ± 4.0	11.1 ± 4.3	11.3 ± 3.9

The above results can be conceived as an innovative approach to metamaterials design. Indeed, we offer simple control mechanisms that allow to easily tailor these nanocomposite's overall effective EM properties. For instance, the superparamagnetic MaNPs induce an FMR absorption process of controllable intensity that can be exploited to induce losses. Also, the nanocomposites' electrical properties can be modified by changing the deposited MaNPs loading

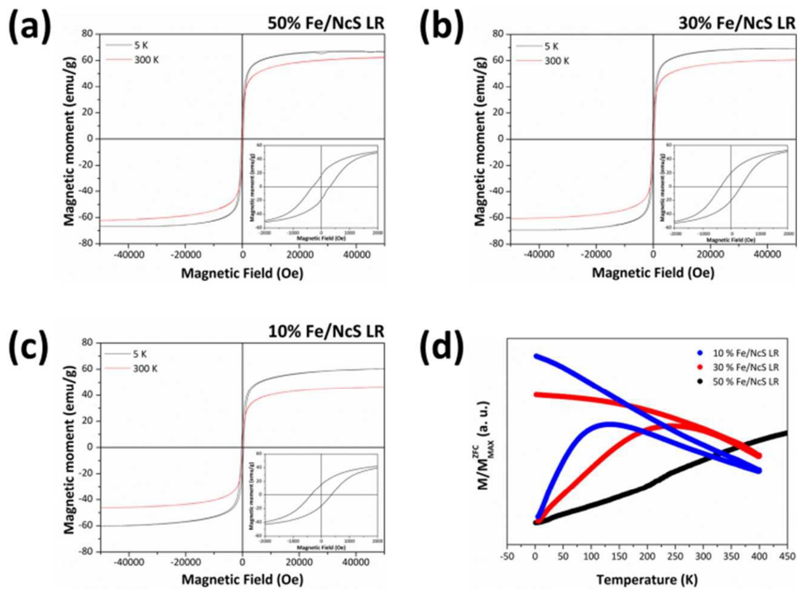

Fig. 13 Magnetization curves recorded against an applied magnetic field for 10% (a), 30% (b) and 50% (c) Fe/NcS LR samples produced with the SOLVA method, and d) against temperature. Insets are M(H) curves recorded at 5 K at low fields.

rate or by choosing a different NcS.

We are currently exploiting these control mechanisms to develop highly efficient ultrathin microwave absorbers [4, 5], by lowering incident microwave reflection and maximizing its absorption rate. We are thus paving the road towards simple and compact metamaterial implementations of stealth and cloaking effects.

Experimental section

Materials

Multi-walled carbon nanotubes (MWCNTs) were obtained from Nanocyl (Belgium). Graphene oxide (GO) and reduced graphene oxide (rGO) were purchased at Nanoinnova Technologies SL (Spain) while graphene nanoplatelets (GNPs) were supplied by TIMCAL (Switzerland). All other reactants were supplied by Sigma Aldrich, Merck, Alfa Aesar or VWR and engaged as received. More details on each reactant are provided in the ESI, section 1.

Synthesis of oxidized multi-walled carbon nanotubes (ox-MWCNTs)

As reported elsewhere [30], 50 mg of MWCNTs were suspended in 100 mL concentrated HNO_3 (65%) and heated, under reflux (100 ºC), for 2 hours under constant magnetic stirring. The resultant product was recovered by filtration over a PTFE membrane filter (Sartorious Stedim Biotech filter type 118, 0.45 μm pore size) and rinsed abundantly with Milli-Q water, until a neutral pH was obtained. Afterwards, it was rinsed once more with 50 mL methanol and dried under vacuum at ambient temperature overnight.

Direct co-precipitation (DCOP) decoration of graphene oxide (GO) as a model nanocarbon solid (NcS) with magnetite nanoparticles (MaNPs).

In a three-necked round bottom flask, 100 mg of GO were suspended in 28 mL Milli-Q water, sonicated for 60 minutes (VWR Ultrasound cleaner 1200-THD, sonication power: 60 W) and deoxygenated under a continuous argon flux for another 60 minutes. In a separate vial, the amounts of $FeCl_3•6H_2O$ and $FeCl_2•4H_2O$ required to achieve a certain Fe/GO (% w/w) loading rate (LR) (e.g. 161 mg and 59 mg of the Fe(III) and Fe(II) salts respectively for a 50% LR) were mixed in a 5 mL glass vial, which then was evacuated thrice using a combination of vacuum/argon cycles. 2 mL of Milli-Q water, previously deoxygenated with an argon current, were then added through a septum producing an aqueous solution of Fe ions with a 0.5 molar ratio of Fe(II)/Fe(III). The latter solution was added dropwise into the graphenic suspension under argon flux and vigorous stirring. The mixture was then stirred for another 24 hours, keeping a controlled argon atmosphere. Afterwards, the solution was heated to 80 ºC and drops of ammonium hydroxide (NH_4OH, 28% w/v aqueous solution) were added until the solution's pH was set to 10. Then, 1.1 mL of hydrazine monohydrate ($N_2H_2•H_2O$) were added and the mixture was refluxed for 5 hours. The obtained product was separated by magnetic decantation, rinsed with Milli-Q water and dried under vacuum, at room temperature, for 12 hours.

Covalent linkage (COV) of MaNPs to graphene oxide (GO) as a model NcS.

In all cases, sonication was performed using a VWR Ultrasound cleaner 1200-THD. Sonication power is specified for each reaction step.

Synthesis of unsupported MaNPs by direct coprecipitation. In a Schlenk flask, 50 mL of Milli-Q water were mixed with 10 mL of a 1M HCl solution and deoxygenated for an hour using a continuous argon flux. 5.46 g of iron (III) chloride hexahydrate (FeCl3•6H2O), 2.01 g of iron (II) chloride tetrahydrate (FeCl2•4H2O) and 600 mg of polyethylene glycol 2000 (PEG-2000) were placed in a second Schlenk flask, which was then purged thrice using a combination of vacuum/argon cycles. By creating vacuum in the second flask, the acidified aqueous solution was transferred from the first flask through a nitrile tube in order to dissolve the powders and produce an oxygen-free aqueous solution of Fe ions with a 0.5 molar ratio of Fe(II)/Fe(III). This solution was then transferred in the same manner to a previously Ar-purged dozer and added dropwise, under argon atmosphere and magnetic stirring, into 100 mL of a 1M sodium hydroxide (NaOH) solution containing 1.00 g of PEG-2000 that had been previously deoxygenated and heated to 60 ºC. A black precipitate formed immediately and once the addition of the iron-containing solution was completed, the dozer was replaced by a spiral cooler and the mixture was stirred for 2 more hours at 60 ºC while being kept under argon atmosphere. Afterwards, the product was separated by magnetic decantation and washed thrice with deoxygenated, Milli-Q water. The resulting product M was dried overnight under vacuum at room temperature and then stored in a glovebox.

Synthesis of magnetite@silica core-shell nanoparticles (M@Si). A solution containing 38 mL Milli-Q water and 160 mL absolute ethanol was deoxygenated for an hour using a continuous argon flux. 160 mg of product M was grinded in the glovebox and then added to the above-mentioned solution. The resulting suspension was sonicated for 2 hours (sonication power: 80 W), after which its pH was set to 12 by using 0.05 mL tetramethylammonium hydroxide (TMAOH), followed by the addition of 4 mL tetraethoxysilane (TEOS). The reaction mixture was magnetically stirred under argon atmosphere for 12 hours at room temperature. The obtained product was separated by magnetic decantation, rinsed ten times, alternating Milli-Q water and ethanol, and dried under vacuum at room temperature for 12 hours.

Functionalization of magnetite@silica core-shell nanoparticles (f-M@Si). In a Schlenk flask, 80 mg of product M@Si were dried overnight under vacuum, at room temperature. 15 mL of freshly distilled toluene were added and the mixture was sonicated for 60 minutes (sonication power: 60 W). Afterwards, 2 mL of (3-aminopropyl)triethoxysilane (APTES) were added through a septum. The suspension was then refluxed at 80ºC for 3 hours. The solid was separated using magnetic decantation, rinsed nine times alternating toluene, methanol and Milli-Q water, and dried under vacuum at room temperature for 12 hours.

Synthesis of an acyl chloride derivative of graphene oxide (GO-Cl). 75 mg of graphene oxide (GO) were placed in a round-bottom flask and sonicated in 40 mL dried toluene (sonication power: 60 W) for an hour. Afterwards, 5.6 mL thionyl chloride ($SOCl_2$) were added and the reaction mixture was refluxed at 120 ºC for 5 hours. The product was filtered, rinsed extensively with toluene and dried overnight under vacuum, at room temperature.

Covalent linkage of functionalized core-shell nanoparticles and graphene oxide acyl chloride derivative (COV). Two vials containing each 2 mL of freshly distilled toluene and 25 mg of f-M@Si or GO-Cl were sonicated for 60 minutes (sonication power: 40 W). Afterwards, both suspensions were mixed and 13 mL of freshly distilled toluene were added. The mixture was then placed under reflux at 100 ºC for 4 hours. The obtained product was magnetically decanted, washed ten times with toluene and dried under vacuum at room temperature for 12 hours.

Solvothermal (SOLV) decoration of different NcS with magnetite nanoparticles.

The different solvothermal methods tested are briefly described hereafter and summarized in Table 2.

SOLV-A Method. 100 mg of a NcS were dispersed into a mixture composed of 27 mL ethylene glycol (EG), 13 mL polyethylene glycol 400 (PEG-400) and 13 mL Milli-Q water. The suspension was sonicated for 2 hours. Afterwards, a certain amount of $FeCl_3•6H_2O$ was added under magnetic stirring in order to obtain the desired Fe/NcS (% w/w) loading rate (LR) (e.g. 242 mg for a 50% LR). After complete dissolution of the salt, crushed NaOH pellets were added until the solution's pH value was set to 13. The mixture was then transferred into a stainless steel autoclave vessel, heated up to 180ºC (approx. 50 minutes) and maintained at that temperature for 23 hours.

SOLV-B Method. 100 mg of a NcS and the required amount of $Fe(acac)_3$ needed to achieve a particular Fe/NcS LR (e.g. 316 mg for a 50% LR) were added to a mixture composed of 10 mL EG and 2 mL Milli-Q water. The mixture was magnetically stirred until dissolution of the $Fe(acac)_3$ complex. Afterwards, it was sonicated for 2 hours. The suspension was transferred into a stainless steel autoclave vessel, heated up to 260 ºC (approx. 80 minutes) and maintained at that temperature for 80 minutes.

SOLV-C Method. 100 mg of a NcS and the required amount of $Fe(acac)_3$ needed to obtain a particular Fe/NS LR (e.g. 316 mg for a 50% LR) were dispersed into 180 mL EG and sonicated for 30 minutes. Afterwards, 80 μL of hydrazine monohydrate ($N_2H_2•H_2O$) were slowly added under magnetic stirring. The suspension was transferred into a stainless steel autoclave vessel, heated up to 180 ºC (approx. 50 minutes) and maintained at that temperature during 15 hours.

SOLV-D Method. 100 mg of a NcS were suspended in 50 mL triethylene glycol (TREG). The suspension was sonicated for 15 minutes. The amount of $Fe(acac)_3$ needed to achieve a particular Fe/NcS LR (e.g. 316 mg for a 50% LR) was added and the mixture was magnetically stirred for 10 minutes. It was then transferred into a stainless steel autoclave vessel, heated up to 260 ºC (approx. 50 minutes) and maintained at that temperature for 40 minutes.

In all the described procedures: a) sonication was performed in a VWR ultrasound cleaner USC 1200-THD at 80 W sonication power); b) the autoclave's temperature was automatically regulated by a Parr 4836 temperature controller (Parr Instrument Company, USA) having an average heating rate of 4 ºC/min; c) the autoclave's inner atmosphere was not purged nor modified in any manner during the synthesis, while the system's pressure was left to build up during heating without any type of external control; d) when the heating time was completed, the autoclave was immediately immersed in an ice bath and cooled down to ambient temperature; and e) the obtained products were separated by magnetic decantation, filtered over a PVDF filter (Millipore GVWP02500, 0.22 μm pore size) and rinsed six times, alternating Milli-Q water and ethanol. Afterwards, they were dried under vacuum, at room temperature for 12 hours.

Characterization

Powder X-ray diffraction (XRD). Samples were introduced into 0.5 mm thin-walled glass capillaries (Hilgenberg GmbH, Germany), mounted on a goniometer head and kept at 200 mm from the detector. Diffractograms were then collected at room temperature using a MAR345 diffractometer (MarResearch GmbH), a Mo-Kα (0.71073 Å) anode and a XENOCS focusing mirror. The obtained 2D diffractograms were azimuthally integrated using the Fit2D software, calibrated with a LaB_6 standard (NIST 660b Standard). Rietveld analysis was performed with the Fullprof crystallographic suite (CNRS, France) using input files obtained from the literature [47, 48].

Scanning electron microscopy with coupled energy-dispersive X-ray spectroscopy (SEM-EDX). Samples prepared for TEM analysis were also used for SEM imaging. The TEM grids were mounted on double-face adhesive carbon tape adhered to an aluminum sample holder. They were analyzed without further preparation in a FEGSEM Ultra55 instrument (Carl Zeiss) equipped with an Oxford Inca EDX system (Oxford Instruments). Images were acquired with the SmartSEM software (Carl Zeiss, Germany) at different acceleration voltages ranging between 3 keV and 15 keV, using InLens and SE2 detectors. X-ray fluorescence spectra were collected at 15 keV using the ESPRIT software (Bruker, Germany).

Scattering matrix (S-parameters) measurements. Samples were mixed with ethanol and introduced into rectangular cavities drilled in the two slots of a coplanar line etched on a RO3010™ substrate, pressing with a spatula to compact the sample slurry. Once completely filled, the as-prepared line was dried under vacuum at 25ºC for 2 hours. A universal testfixture 36801K was used to connect the loaded line to an Anritsu 37369A 40 GHz vector network analyzer (VNA). A variable external field was applied using an electromagnet NTM 10400M-260. Data acquisition was performed using Labview and the obtained measurements were normalized using a standardized Matlab background subtraction technique, in order to remove spurious losses induced by connectors and substrate.

Superconducting Quantum Interference Device (SQUID) magnetometer. Magnetization measurements were performed using a Quantum Design MPMS-XL5 SQUID magnetometer without any further sample preparation. Magnetization curves as a function of an applied magnetic field (M(H) curve) were measured at 5 K and 300 K after applying a subsequent degaussing procedure. The magnetization was then measured at constant temperature by sweeping the magnetic field from +7 T to -7 T, and then from -7 T to +7 T. Temperature dependent magnetization (M(T)) curves were recorded as follows: the sample was introduced in the SQUID at room temperature and cooled down to 5 K with no applied field (zero field cooled (ZFC) curve) after applying a careful degaussing procedure. A magnetic field of 7.5 mT was applied, and the M(T) curve was recorded upon heating from 5 to 400 K. The sample was then cooled down to 5 K under the same applied field (field cooled (FC) curve), and the M(T) curve was recorded upon heating from 5 to 400 K.

Transmission electron microscopy (TEM). Samples were dispersed in hexane by sonication. Three drops of the supernatant were then deposited onto a holey carbon film supported on a copper grid (C-flat, Protochips, USA), and left to dry, overnight, at room temperature under vacuum. TEM images were obtained on a LEO 922 OMEGA Energy Filter Transmission Electron Microscope operating at 200 kV. Measurements of particle size were executed with the AnalySIS Auto 5.0 software (Olympus Soft Imaging Solutions GmbH, Germany) on at least 100 particles per sample as recorded on the TEM images.

Thermogravimetric analysis (TGA). Samples (5-10 mg) were placed in alumina containers and introduced into a Mettler Toledo TGA/SDTA 851e instrument. Thermograms were recorded up to 900ºC using a 10 °C/min heating rate under a air flux. The samples were recovered after heating and analyzed by XRD as described above, identifying in all cases a pure hematite (Fe_2O_3) phase. TGA data treatment required for the calculation of the Fe/NcS loading rates was based on the molecular weight of this particular iron oxide phase. Corrections for residual non-carbonaceous impurities present in the different NcS were also included in these calculations.

X-Ray photoelectron spectroscopy (XPS). A few milligrams of each sample were deposited on a double-sided adhesive support clung onto a brass cup, and then introduced onto a Macor® carousel. The analyses were performed on a SSX 100/206 photoelectron spectrometer from Surface Science Instruments (USA) equipped with a monochromatized micro focused Al X-ray source (powered at 20 mA and 10 kV). The pressure in the analysis chamber was around 10^{-6} Pa. A flood gun set at 8 eV and a Ni grid placed 3 mm above the sample surface were used for charge stabilisation. The C-(C,H) component of the C1s peak of carbon was fixed to 284.8 eV to set the binding energy scale. Data treatment was performed with the CasaXPS program (Casa Software Ltd, UK). Spectra were decomposed with the least squares fitting routine provided by the software with a Gaussian/Lorentzian (85/15) product function and after subtraction of a Shirley-type baseline [49]. Molar fractions were calculated using peak areas normalised on the basis of acquisition parameters and sensitivity factors provided by the manufacturer.

Conclusions

The synthesis and characterization of nanocarbon solids decorated with magnetite nanoparticles (MaNPs) was thoroughly studied. When comparing the results obtained by the direct co-precipitation, solvothermolysis and covalent bonding techniques, we have demonstrated that each synthetic method produces a MaNPs@GO nanocomposite with different characteristics. To the best of our knowledge, it is the first time that such a systematic comparison is performed. Considering our intended applications, the direct co-precipitation technique presents two main drawbacks: the difficulty of reproducibly controlling the nanocomposite's final composition, and consequently its electromagnetic properties; and the relatively heterogeneous and highly stacked spatial distribution of the MaNPs over the graphenic surface. As for the covalent linkage method, it is interesting to note that it has not been as extensively explored in the literature. This might be partly due to the higher amount of experimental manipulations it requires in order to achieve the final product, particularly when compared to the solvothermal method. Another possible reason could be that the results published this far, mostly based on FTIR studies, were not firmly conclusive about the formation of a covalent bond between the graphenic surface and the MaNPs. Nevertheless, the principal drawback of this method seems to be the obtention of large, micrometric MaNPs agglomerates, coexisting independently along with the desired nanocomposites and which, under the experimental conditions used, are impossible to isolate. These agglomerates can locally and uncontrollably alter the end materials' effective electrical permittivity (ε) and magnetic permeability (μ) values, making it virtually impossible to obtain a nanocomposite material with a reproducible and homogeneous set of EM properties. Considering the above, we consider that the solvothermal route has an overall increased performance.

Accordingly, the in-depth study of the polyol solvothermal methodology led us to identify a series of critical factors governing the decoration of different nanocarbon solids that had been not been stressed out before. Regarding the deposited MaNPs chemical identity, morphology and particle size, we have proven that, besides reaction time and temperature, the choice of the iron precursor, the reaction system's water content and the oxidation degree of the NcS all play a fundamental role. Indeed, producing MaNPs by decomposing an iron complex in the absence of water produces minute nanoparticles whose sizes are below 3 nm. Interestingly, we have shown that by solely adding 20% of water to the reaction system, we have almost doubled the obtained MaNPs size. Also, we have proven that a higher number of oxygenated functions diminishes the MaNPs sizes as well as distributes them more evenly over the NcS surface.

We have also demonstrated that the amount of MaNPs that can be loaded onto the NcS seems to rely upon the nature of the iron precursor, the type of NcS and its oxidation state. Ours results show that a lower Fe/NcS LR was systematically obtained when the Fe(acac)$_3$ complex was used as an iron precursor, possibly due to the fact that it was only partially decomposed under the experimental conditions used. This drawback could be overcome by using reaction temperature higher than 260 ºC and longer reaction times. Nonetheless, these modifications could also have an impact on the MaNPs size distribution. We have also proven that as the NcS is more oxidized, a larger amount of MaNPs can be loaded. We believe that this is due to the establishment of electrostatic interactions between the oxygenated functions found on the NcS and the ionic iron species found in solution, especially at the higher pH values used in some of our tested methods.

Finally, we have characterized the nanocomposite's magnetic properties, obtaining results that are characteristic for ferrimagnetic iron oxide nanoparticles in a superparamagnetic state. Furthermore, we were able to prove that our nanocomposites are microwave active. Indeed, we have shown that a series of FMR absorption processes are induced by the deposited MaNPs. By analyzing the nature of these absorption processes, we have proven that this is undoubtedly an FMR phenomenon. Consequently, we have determined that the MaNPs induce a natural or zero-field resonance to be found around 4 GHz. We have also shown that the amount of loaded MaNPs has an important effect on the intensity of the FMR phenomenon as well as on the nanocomposites' electrical properties. Finally, we have demonstrated that these electrical properties can be further modified by changing the NcS type. In consequence, the overall EM properties of these metamaterial nanocomposites can be easily tuned, being excellent candidates for the production of highly effective microwave absorbers for shielding applications.

Acknowledgements

The authors are grateful to the National Fund for Scientific Research (F.R.S.-FNRS) for supporting this research. This work is also supported by the MINATIS project co-funded by the European Regional Development Fund (ERDF) and the Walloon region, and by the Communauté Française de Belgique, through the project "Nano4waves" funded by its research program "Actions de Recherche Concertées".

Notes and references

1 F. Bilotti, and L. Sevgi, *Int. J. RF Microw. C.E.* 2012, **22** (4), 422-438.

2 C. M. Soukoulis and M. Wegener, *Nat. Photonics,* 2011, **5**, 523-530.

3 D. R. Smith, W. J. Padilla, D. C. Vier, S. C. Nemat-Nasser and S. Schultz, *Phys. Rev. Lett.*, 2000, **84**, 4184-4187.

4 Y. Danlée, I. Huynen and C. Bailly, *Appl. Phys. Lett.,* 2012, **100**, 213105.

5 N. I. Landy, S. Sajuyigbe, J. J. Mock, D. R. Smith, and W. J. Padilla. *Phys. Rev. Lett.,* 2008, **100**(20), 207402.

6 D. Schurig, J.J. Mock, B.J. Justice, S.A. Cummer, J.B. Pendry, A.F. Starr and D.R. Smith, *Science,* 2006, **314**, 977-980.

7 H. Chen, *J. Mater. Chem*., 2011, **21**, 6452-6463.

8 F. Bilotti and L. Sevgi, Int. *J. RF Microw. C.E.*, 2012, **22**(4), 422-438.

9 H. M. Mesfin, A.C. Baudoin, S. Hermans, A. Delcorte, I. Huynen, C. Bailly, *Appl. Phys. Lett.,* 2014, **105**, 103105.

10 X. Huang, X. Zhou, K. Qian; D. Zhao, Z. Liu and C. Yu, *J. Alloy Compd.*, 2012, **514**, 76-80.

11 B. Li. H. Cao, J. Shao, M. Qu, and J. H. Warner, *J. Matter. Chem.,* 2011, **21**, 5069.

12 Q. Wang, L. Jiao, H. Du, Y. Wang and H. Yuan, *J. Pow. Sour.,* 2014, **245**, 101-106.

13 H. Wu, G. Gao, X. Zhou, Y. Zhang, and S. Guo, *Cryst. Eng. Comm.*, 2012, **14** (2), 499-504.

14 F. He, J. Fan, D. Ma, L. Zhang, C. Leung, H. L. Chan, *Carbon*, 2010, **48**, 3139-3144.

15 Y. Yao, S. Miao, S. Liu, L.P. Ma, H. Sun and S. Wang, *Chem. Eng. J.,* 2012, **184**, 326-332.

16 X.Y. Yang, Z.Y. Zhang, Y.F. Ma, Y. Huang, Y.S. Wang and Y.S. Chen. *J. Mater. Chem.*, 2009, **18**, 2710.

17 H. Teymourian, A. Salimi and S. Kherzrian, *Biosens Bioelectron*, 2013, **49**, 1-8.

18 Y. Zhan, F. Meng, Y. Lei, R. Zhao, J. Zhong, and X. Liu, *Mater. Lett.*, 2011, **65**, 1737-1740.

19 a) P. Liu, Y. Huang and X. Zhang, *J. Alloy Compd.*, 2014, **596**, 25-31; b) P. Liu, Y. Huang and X. Zhang, *Mater Lett.*, 2014, **129**, 25-31

20 X. Shen, J. Wu, S. Bai and H. Zhou, *J. Alloy Compd.*, 2010, **506**, 136-140.

21 J. Deng, X. Wen, Q. Wang, *Mater. Res. Bull.*, 2012, **47**, 3369-3376.

22 J. Wan, W. Cai, J. Feng, X. Meng and E. Liub, *J. Mater. Chem.*, 2007, **17**, 1188

23 P. Liu, W. Zhong, Z. Wu, J. Qiu, *Chem. Eng. J.,* 2013, **219**, 10-18.

24 Y. Zhan, Z. X. Yang, F. Meng, J. Wei, R. Zhao and X. Liu, *J. Colloid Interf. Sci.*, 2011, **363**, 98-104.

25 W. Baaziz, L. Truong-Phuoc, C. Duong-Viet, G. Melinte, I. Janowska, V. Papaefthimiou, O. Ersen, S. Zafeiratos, D. Begin, S. Begin-Colin and C. Pham-Huu, *J. Mater. Chem. A.,* 2014, **2**, 2690-2700.

26 Y. Li, J. Chu, J. Qi and X. Li, *Appl. Surf. Sci.*, 2011, **257**, 6059-6062.

27 W. Baaziz, B.P. Pichon, S. Fleutot, Y. Liu, C. Lefevre, J.M. Greneche, M. Toumi, T. Mhiri and S.Begin-Colin, *J. Phys. Chem. C*, 2014, **118** (7), 3795–3810.

28 J. Guo, R. Wang, W.W. Tjiu, J. Pan, and T. Liu, *J. Hazard. Mater.,* 2012, **225-226**, 63-73.

29 V. Singh, D. Joung, L. Zhai, S. Das, S. Khondaker and S. Seal, *Prog. Mater. Sci.,* 2011, **56**, 1178-1271.

30 S. Hermans, V. Bruyr and M. Devillers, *J. Mater. Chem.*, 2012, **22**, 14479.

31 I. Martínez-Mera, M.E. Espinosa-Pesqueira, R. Pérez-Hernández and J. Arenas-Alatorre, *Mater. Lett.*, 2007, **61**, 4447-4451.

32 R. Massart, and V. Cabuil, *J. Chim. Phys.*, 1987, **84** (7-8), 967-973.

33 Cornell, R.M. and Schwertmann, U. (2003) The iron oxides. Structure, properties, reactions, occurrences and uses (2nd ed). Wiley-VCH; Darmstadt, Germany. 664 pp.

34 M.E. Mendoza, F. Donado, R. Silva, M.A. Pérez. and J.L. Carrillo, *J. Phys. Chem. Solids*, 2005, **66**, 927-931.

35 S. Qu, H. Yang, D. Ren, S. K, G. Zou, S. Li and M. Li, *J. Colloid Interf. Sci.*, 1999, **215**, 190-192.

36 B. Konkena and S. Vasudevan, *J. Phys. Chem. Lett*., 2012, **3**, 867-872.

37 S. E. Skrabalak, B. J. Wiley, M. Kim, E. V. Formo and Y. Xia, *Nano Lett.,* 2008, **8**(7), 2077-2081.

38 J. Zhou, H. Song, L. Ma and X. Chen, *RSC Adv.,* 2011, **1**, 782-791.

39 P. Han, H. Wang, Z. Liu, X. Chen, W. Ma, J. Yao, Y. Zhu and G. Cui. *Carbon,* 2011, **49**, 693-700.

40 W. Baaziz, B.P. Pichon, S. Fleutot, Y. Liu, C. Lefevre, J.M. Greneche, M. Toumi, T. Mhiri and S. Begin-Colin. *J. Phys. Chem. C* 2014**, 118** (7), 3795.

41 D. Toulemon, B.P. Pichon, X. Cattoen, M.W.C. Man and S. Begin-Colin. *Chem. Commun.,* 2011**, 47** (43), 11954.

42 Y. Zhan, F. Meng, Y. Lei, R. Zhao, J. Zhong and X. Liu. *Mater Lett.*, 2011, **65**, 1737-1740.

43 P. Liu, Y. Huang and X. Zhang, *J. Alloy Compd.*, 2014, **617**, 511-517.

44 G. Li, L. Wang, W. Li and Y. Xu. *RSC Adv.*, 2015, **5**, 8248-8257.

45 C. Kittel, *Phys. Rev.*, 1948, **73** (2), 155-161.

46 M. Charilaou, K.K. Sahu, D. Faivre, A. Fischer, I. García-Rubio A.U. and Gehring. *Appl. Phys. Lett.,* 2011, **99**, 182504.

47 M.E. Fleet, *J. Solid State Chem.*, 1986, **62**(1), 75-82.

48 F. Fajaroh, H. Setyawan, A. Nur, and I.W. Lenggoro, *Adv. Powder Technol.,* 2013, **24**, 507-511.

49 D.A. Shirley *Phys. Rev.*, 1972, **B5**, 4709-4714.

Decoration of nanocarbon solids with magnetite nanoparticles: towards microwave-responsive metamaterials

Francisco Mederos-Henry[a], Benoît P. Pichon[b], Yzaora Tchuitio Yagang[a], Arnaud Delcorte[c], Christian Bailly[c], Isabelle Huynen*[d] and Sophie Hermans*[a]

Graphical abstract

Image:

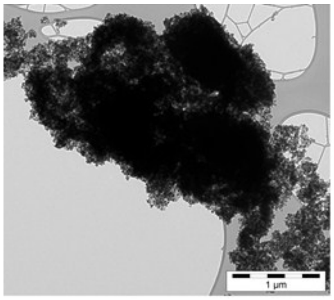

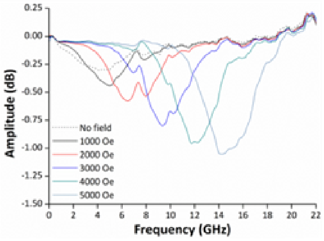
FMR response of magnetite / rGO nanocomposite as powder:

Text:

Nanocarbon supports were decorated with magnetite nanoparticles (MaNPs) using three different methods. The MaNPs where shown to induce a ferromagnetic resonance (FMR) phenomenon in the obtained nanocomposites, imparting a natural or zero-field resonance around 4 GHz.